

A Journal of the Gesellschaft Deutscher Chemiker

Angewandte

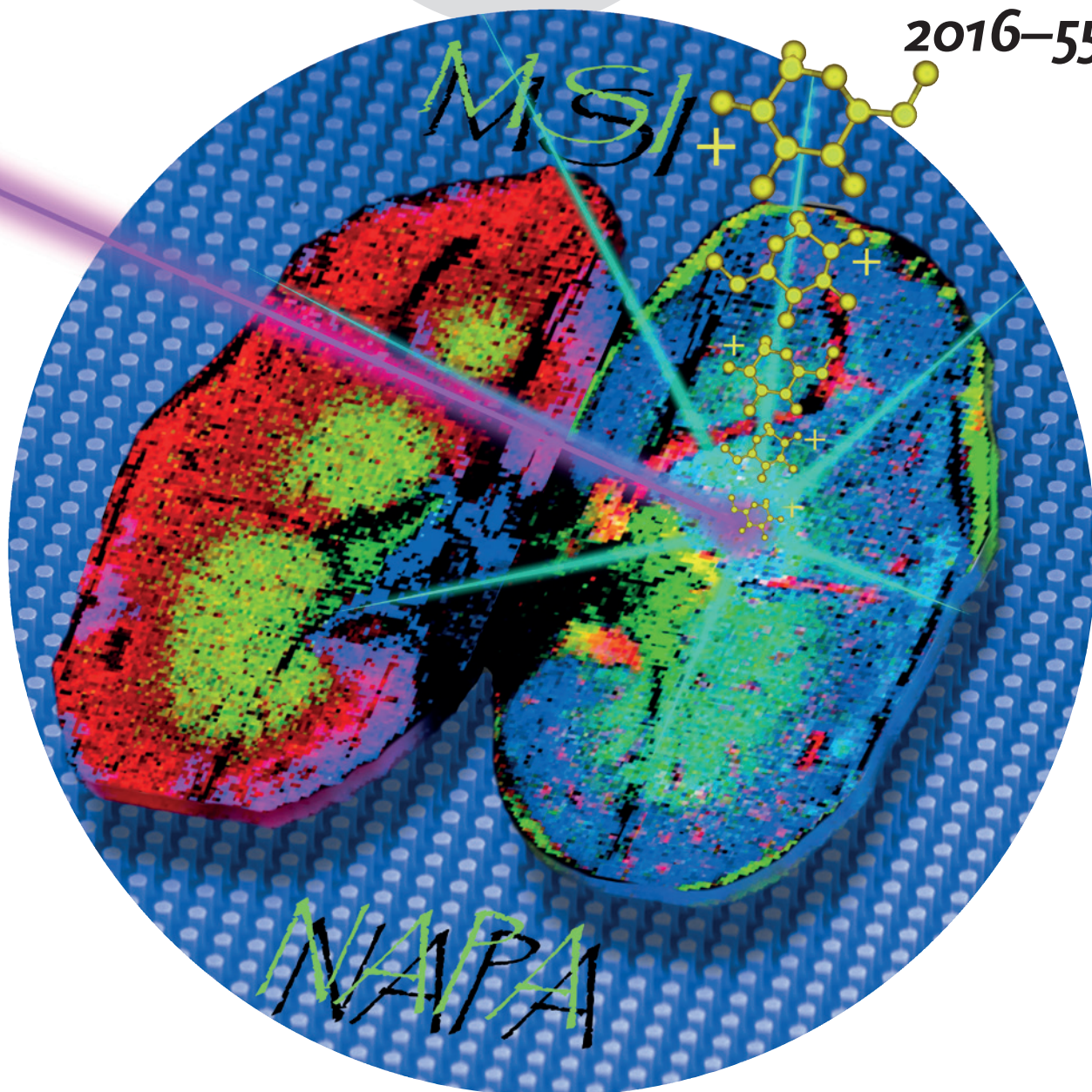
GDCh

International Edition

Chemie

www.angewandte.org

2016–55/14



Cover Picture

A. Vertes *et al.*

Molecular Imaging of Biological Samples on Nanophotonic Laser
Desorption Ionization Platforms

Mass Spectrometry Imaging

International Edition: DOI: 10.1002/anie.201511691

German Edition: DOI: 10.1002/ange.201511691


Molecular Imaging of Biological Samples on Nanophotonic Laser Desorption Ionization Platforms

Sylwia A. Stopka, Charles Rong, Andrew R. Korte, Sridevi Yadavilli, Javad Nazarian, Trust T. Razunguzwa, Nicholas J. Morris, and Akos Vertes*

Abstract: Mass spectrometry imaging (MSI) is a comprehensive tool for the analysis of a wide range of biomolecules. The mainstream method for molecular MSI is matrix-assisted laser desorption ionization, however, the presence of a matrix results in spectral interferences and the suppression of some analyte ions. Herein we demonstrate a new matrix-free MSI technique using nanophotonic ionization based on laser desorption ionization (LDI) from a highly uniform silicon nanopost array (NAPA). In mouse brain and kidney tissue sections, the distributions of over 80 putatively annotated molecular species are determined with 40 μm spatial resolution. Furthermore, NAPA-LDI-MS is used to selectively analyze metabolites and lipids from sparsely distributed algal cells and the lamellipodia of human hepatocytes. Our results open the door for matrix-free MSI of tissue sections and small cell populations by nanophotonic ionization.

Molecular distributions in cells and tissues, in correlation with anatomical features, can provide insight into disease mechanisms, facilitate clinical diagnosis, and reveal the localization of pharmaceuticals. In recent years, new mass-spectrometry-based technologies have been developed for the spatial mapping of metabolites, lipids, proteins, and xenobiotics in tissue sections.^[1,2] Targeted techniques, such as autoradiography and histological staining, require radioactive or fluorophore labeling resulting in a limited number of analytes that can be visualized in a single experiment.^[3] In contrast, mass spectrometry imaging (MSI) can simultaneously provide spatial distributions for hundreds of metabolites, lipids, proteins, and drugs in a non-targeted fashion.^[4,5]

Among the established vacuum-based ionization methods, secondary ion mass spectrometry (SIMS)^[6] and matrix-assisted laser desorption ionization (MALDI)^[7–9] have been extensively applied for MSI, single cell, and subcellular analysis. In most implementations, SIMS does not require a matrix and can achieve < 100 nm spatial resolution, how-

ever it is known to induce a considerable amount of fragmentation for large molecules. In contrast, MALDI requires the addition of an organic matrix that can contribute to ion suppression and spectral interferences in the low mass range. Emerging atmospheric-pressure MSI techniques, including desorption electrospray ionization (DESI)^[10] and laser ablation electrospray ionization (LAESI) allow for direct tissue imaging with minimal sample preparation but typically provide limited spatial resolution.^[11]

To overcome the challenges associated with matrix heterogeneity and interferences in the low m/z region, a significant number of matrix-free LDI techniques have been introduced.^[12] Despite the large variety of these platforms (surface-assisted LDI (SALDI)),^[13] carbon nanotubes,^[14] porous alumina,^[15] platinum nanoflowers,^[16] diamond nanowires,^[17] nanostructured gold thin film,^[18] and zinc, tungsten, and rhenium oxide nanoparticles^[19,20], only a few of them, for example, desorption ionization on porous silicon (DIOS),^[21,22] and nanostructure initiator mass spectrometry (NIMS)^[23] have been broadly explored for MSI. In a limited number of applications, other matrix-free techniques, including LDI from laser engineered graphene paper,^[24] carbon-substrate-assisted LDI,^[25] silica plate imprinting followed by LDI,^[26] nanowire-assisted LDI (NALDI),^[27] and SALDI,^[28,29] were also explored for MSI. The most tested system among these platforms, NIMS, was demonstrated for tissue and cell imaging.^[30–33]

Earlier studies showed that silicon nanopost array (NAPA) structures, produced with precise control over the height, diameter, and periodicity of the posts, could be optimized for enhanced LDI yields.^[34–37] For example, adjusting the aspect ratio of the nanoposts resulted in extreme sensitivity with a limit of detection in the zeptomole range, and a dynamic range of over three orders of magnitude, whereas imprecisions in the periodicity had negligible influence.^[36] The ultratrace detection and quantitation capabilities of NAPA provided insight into metabolic changes in single yeast cells induced by oxidative stress.^[38] These features indicate that the NAPA substrate is an appealing candidate for MSI.


In nanophotonic ionization, the geometrical features of the nanostructure are commensurate with the wavelength of the laser light used to induce LDI. This results in a unique interaction between the nanostructure and the laser radiation. The two most important consequences of nanophotonic ionization are the polarization dependence of the ion yield^[39] and the ability to adjust the internal energy of the produced ions through the laser fluence.^[40] These unique features of NAPA provide opportunities to control the ion

* S. A. Stopka, C. Rong, Dr. A. R. Korte, Prof. A. Vertes

Department of Chemistry
The George Washington University
Washington, DC 20052 (USA)
E-mail: vertes@gwu.edu

Dr. S. Yadavilli, Dr. J. Nazarian
Research Center for Genetic Medicine, Children's National Medical
Center, Washington, DC 2001 (USA)

Dr. T. T. Razunguzwa, Dr. N. J. Morris
Protea Biosciences Inc. Morgantown, WV 26505 (USA)

 Supporting information and the ORCID identification number(s) for the author(s) of this article can be found under <http://dx.doi.org/10.1002/anie.201511691>.

yield of the LDI process and the internal energy of the produced ions that offer new opportunities in imaging experiments.

To produce larger NAPA surfaces required for MSI, the earlier patterning technology, based on electron-beam lithography, was replaced by deep UV projection lithography, a high throughput nanofabrication method.^[37] This nanoprecise fabrication technique produced NAPA substrates that were uniform throughout an entire wafer (ca. 100 mm in diameter), and exhibited heterogeneity only on the submicrometer scale.

Herein we demonstrate the first molecular imaging experiments using LDI-MS from silicon NAPA for the detection and spatial mapping of metabolites and lipids in various biological samples, for example, tissue sections. The ability to selectively target thin cellular features by LDI from NAPA is utilized for the metabolic analysis of lamellipodia. The mechanism of material removal in NAPA-LDI-MSI is illuminated by scanning electron microscope (SEM) observations of the pores in the tissues produced by the underlying nanoposts heated by laser radiation.

To demonstrate MSI capabilities from NAPA, 10 μm coronal sections (0.3 to 0.9 mm anterior from bregma) of mouse brain tissue were transferred by thaw-mounting onto NAPA chips and imaged in positive and negative ion modes (Figure 1). As shown in Figure S1 in the Supporting Informa-

and NIMS imaging is performed at around 100 mJ cm^{-2} .^[31,41] Overall, the need for thinner sections or higher fluences for NIMS suggests that desorption is more efficient from NAPA structures.

A total of 80 metabolites and lipids were putatively annotated and spatially mapped from a coronal mouse-brain section (see Table S1 and S2). For example, the negative ion at m/z 888.6258 assigned as $[\text{ST}(24:1)-\text{H}]^-$ and $[\text{eicosenoic acid}-\text{H}]^-$ appearing at m/z 309.2795 were more abundant in the corpus callosum (CC) and the anterior commissure (aco), whereas the ion at m/z 718.5453, corresponding to $[\text{PE}(34:0)-\text{H}]^-$, was localized to the caudoputamen (CP) and the cortex (see panels b–f in Figure 1).

To ascertain that the MSI signal was directly correlated with the NAPA substrate, a brain section was deposited at the interface between the chip and the unprocessed silicon wafer (see panels g–l in Figure 1). The molecular images clearly show that the presence of the NAPA structure is required for signal generation.

To determine the spatial resolution of tissue imaging by NAPA-LDI-MSI, a 10 μm section of the cerebellum was mapped using oversampling with 25 μm step size and a laser fluence of around 100 mJ cm^{-2} (see Figure S2). Anatomical features of the arbor vitae fiber tracts from the granular layers were discernable in the optical microscopy images (see Figure S2a). Molecular imaging on NAPA (Figure S2b)

revealed spatial resolution of approximately 40 μm . The main reason behind the modest spatial resolution was the laser focal spot size in the commercial instrument. Based on the high sensitivity provided by the NAPA structures and the uniform post distribution, with better focusing, a submicrometer spatial resolution seems ultimately achievable. Direct comparison with MALDI-MSI (see Table S3) indicates that currently this long-established technique offers better ultimate spatial resolution but the dynamic range of quantitation by NAPA is greater.

Surface characterization of the tissue sections after laser exposure by SEM showed the development of distinct pores (see Figure 2). The pores exhibited average diameters

and periodicities of 146 ± 19 nm and 332 ± 36 nm, respectively that closely matched the 150 nm diameter and 337 nm periodicity of the nanoposts. This observation provided insight into the mechanism of ion production from thin tissue sections resting on a NAPA structure. Nanophotonic interactions between the silicon structure and the laser irradiation result in fast heating of the posts.^[34,42] The hot tips of the posts induce rapid local evaporation resulting in volatilization of the tissue material. Ionization of adsorbates on NAPA upon laser irradiation has been attributed to the enhanced electromagnetic field in the tip region. Our results

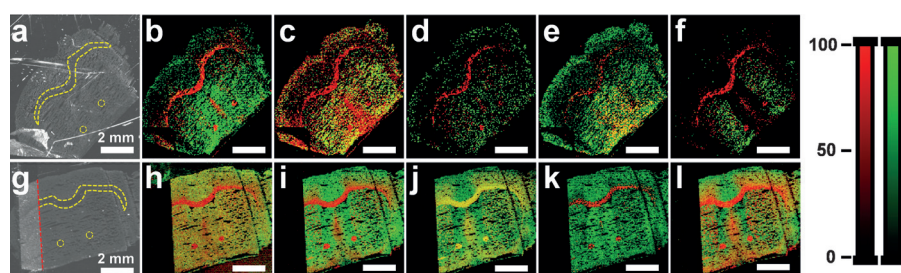


Figure 1. a) Optical image of coronal mouse brain tissue section on a NAPA chip before LDI-MSI. Combined distributions of b) $[\text{ST}(24:1)-\text{H}]^-$ and $[\text{PE}(P-38:4)-\text{H}]^-$, c) $[\text{octadecenoic acid}-\text{H}]^-$ and $[\text{PE}(P-38:6)-\text{H}]^-$, d) $[\text{eicosenoic acid}-\text{H}]^-$ and $[\text{PE}(34:0)-\text{H}]^-$, e) $[\text{docosatetraenoic acid}-\text{H}]^-$ and $[\text{docosahexaenoic acid}-\text{H}]^-$, and f) $[\text{PE}(P-18:2/18:1)-\text{H}]^-$ and $[\text{PE}(36:4)-\text{H}]^-$ derived from negative-ion spectra and presented on (red) and (green) false color scales, respectively. g) Optical image of coronal mouse brain tissue section on a NAPA chip before LDI-MSI. Red line indicates the edge of the NAPA chip. Composite distributions of h) $[\text{cholesterol}-\text{H}_2\text{O} + \text{H}]^+$ and $[\text{DG}(P-32:1) + \text{H}]^+$, j) $[\text{PI}-\text{Cer}(18:0/18:0) + \text{H}]^+$ and $[\text{PC}(32:0) + \text{K}]^+$, j) $[\text{PC}(18:0/16:1) + \text{Na}]^+$ and $[\text{PA}(38:2) + \text{K}]^+$, k) $[\text{PI}-\text{Cer}(40:0) + \text{H}]^+$ and $[\text{PE}(P-40:6) + \text{K}]^+$, and l) $[\text{PI}-\text{Cer}(38:0) + \text{H}]^+$ and $[\text{PE}(38:6) + \text{K}]^+$ from positive-ion spectra presented on (red) and (green) false color scales, respectively.

tion, the mass spectra in both ion modes showed high signal-to-noise ratios with very low interference from the background. After de-isotoping, the negative- and positive-ion spectra contained 163 and 198 different ionic species, respectively. The laser fluence required for desorption of a 10 μm thick sample on a NAPA substrate was approximately 100 mJ cm^{-2} . In comparison, for a 12 μm mouse-embryo section the original version of NIMS needed a laser etching step with 400 mJ cm^{-2} fluence followed by NIMS analysis at 10 mJ cm^{-2} .^[23] More recently, the need for laser etching has been eliminated by cutting thinner tissue sections (2–4 μm)

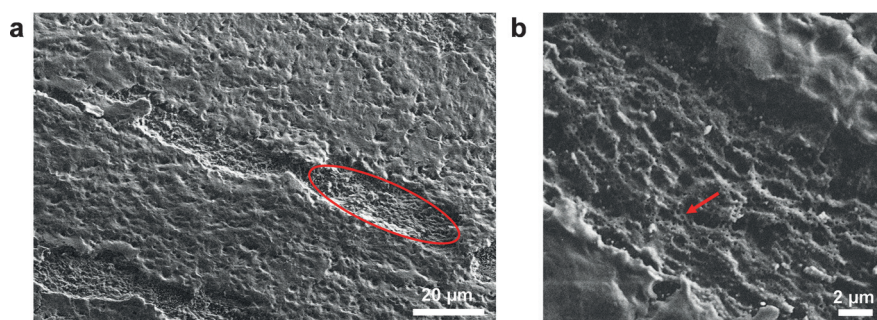


Figure 2. a) An SEM image of a 10 μm thick coronal mouse-brain section on a NAPA chip after exposure to 10 laser pulses per position at a fluence of 100 mJ cm^{-2} . Step size between the exposed areas is 50 μm . The altered tissue as a result of laser desorption in a single pixel is highlighted by a red ellipse. b) Higher-magnification SEM image showing pores (see arrow) generated by tissue removal as a result of the hot nanoposts heated by the laser radiation.

also show the uniformity of ion generation down to submicrometer scale, however owing to the uncontrolled relative position between the nanoposts and tissue features, selective sampling cannot be achieved on that scale.

To investigate the versatility of nanophotonic structures as an imaging platform, another tissue type with higher tensile strength, and cell deposits from an algal culture were subjected to NAPA-LDI-MSI. A 10 μm sagittal mouse-kidney section was mounted onto a NAPA chip and imaged in positive ion mode (Figure 3). Imaging of the algal cells is discussed in the Supporting Information. Localization of certain metabolites and lipids in the kidney section was apparent from higher ion abundances from specific anatomical regions. For example, as shown in Figure 3b, the heme b cation at m/z 616.1771 was detected primarily from the vascular features of the kidney, including capillaries, clearly visible in the composite image in Figure 3e. The ion assigned as $[\text{PE}(40:8) + \text{K}]^+$ at m/z 826.4779 was mainly localized to the renal medulla and the lipid ion $[\text{PC}(32:0) + \text{K}]^+$ was detected mainly in the renal cortex (Figure 3c,d). Similar to mouse brain imaging, the mass spectrum from the kidney (see Figure S3) did not show background interferences.

Subcellular variations in composition are masked when chemical analysis is carried out on entire cells. Many cells contain structures known as lamellipodia that are responsible

for cell motility and extend from the cell body as an approximately 0.2 μm thin layer of cytoplasm at the front end of a moving adherent cell.^[43] Analysis of metabolites and lipids in these thin cellular structures is a largely unexplored field.

To explore the capability of NAPA-LDI-MS for the analysis of lamellipodia, HepG2/C3A human hepatocarcinoma cells were cultured directly on NAPA chips. (Invertebrate neurons had been cultured and analyzed on DIOS chips.^[44]) After six days of incubation, SEM imaging revealed the attachment of the cells to the nanoposts (Figure S4). Owing to the large difference in thickness between the cell body

and the lamellipodia, at moderate fluences the laser radiation can only heat up the underlying nanoposts for the lamellipodia, and facilitate rapid vaporization of the thin cellular material. (The cell body can also be analyzed at higher laser fluences.) Indeed, observations by SEM after irradiation at a laser fluence of about 24 mJ cm^{-2} revealed small pores where the posts touched the lamellipodia (see Figure 4a). From the lamellipodia, among other ions $[\text{phosphocholine} + \text{H}]^+$, $[\text{glucose} + \text{Na}]^+$, $[\text{cholesterol-H}_2\text{O} + \text{H}]^+$, $[\text{TG}(50:8) + \text{K}]^+$, and $[\text{PE}(38:4) + \text{K}]^+$ were detected. For clusters of 12 cells, irradiation at a fluence of approximately 24 mJ cm^{-2} gave rise to 27 peaks in the mass spectrum (see Figure 4b) that after background subtraction, de-isotoping, and discounting the molecular adducts corresponded to 13 cellular components.

These results demonstrate the first applications of NAPA-LDI-MS for putative annotation and imaging of over 80 molecular species in animal organ sections and microbial cell deposits. Analysis of 13 metabolites and lipids from lamellipodia was made possible by the selective heating of the nanoposts under these thin structures. These examples show the utility of nanophotonic ion production from biological specimens through the interactions of nanopost arrays and laser radiation. Future work can explore the possibility of selective interactions between nanostructures and cells for

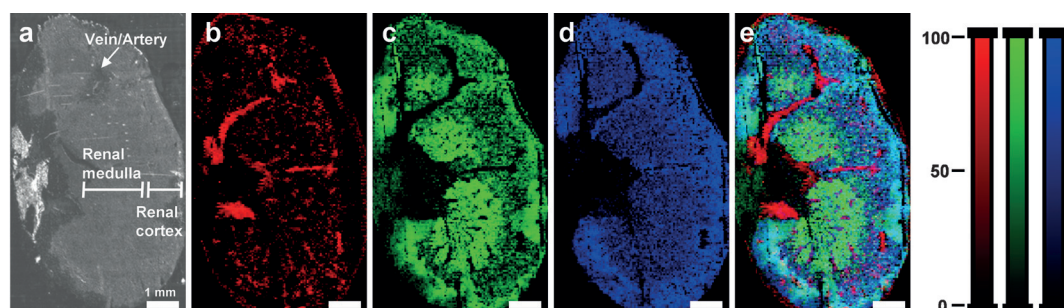


Figure 3. a) Optical image of a 10 μm thick mouse kidney section deposited on a NAPA chip. Spatial distributions of b) $[\text{heme b}]^+$, c) $[\text{PE}(40:8) + \text{K}]^+$, d) $[\text{PC}(32:0) + \text{K}]^+$ produced by NAPA-LDI-MSI. The $[\text{PE}(40:8) + \text{K}]^+$ and $[\text{PC}(32:0) + \text{K}]^+$ correlate with the renal medulla and the cortex, respectively. Veins, arteries, and capillaries are clearly visible in e) the composite plot including all three ions.

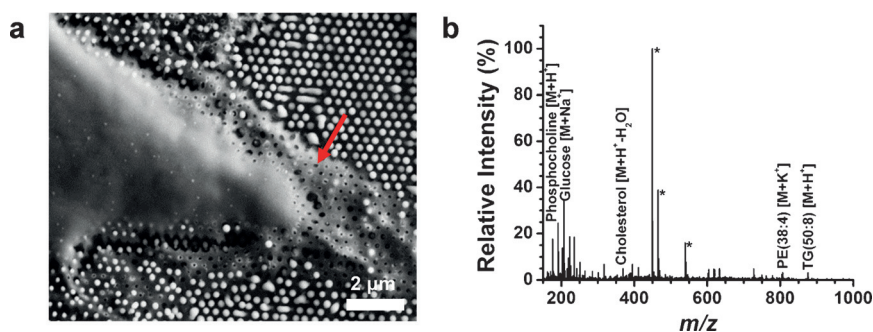


Figure 4. a) SEM image of a HepG2/C3A cell on NAPA, exposed to approximately 24 mJ cm^{-2} laser fluence, with pores (see arrow) in the lamellipodia induced by the irradiated nanoposts. b) Corresponding mass spectrum indicates metabolite and lipid ions originating selectively from the lamellipodia. Background ions from NAPA are marked by *.

molecular analysis and imaging. Molecular imaging of disease biomarkers and drug candidate distributions in tissue sections can also benefit from this matrix free platform.

Experimental Section

Nanofabrication of the NAPA substrate involved deep UV projection lithography and deep reactive ion etching on low resistivity, p-type silicon wafers. The produced nanoposts had dimensions of 150 nm in diameter, 337 nm periodicity, and a height of 1100 nm. Typical imaging chips were $25 \times 25 \text{ mm}^2$ in size and comprised of 5.5×10^9 posts. Biological tissue sections and other samples were transferred onto the NAPA platform for LDI-MS analysis. All experiments were performed using a LTQ-Orbitrap XL mass spectrometer equipped with an intermediate pressure MALDI ion source. The laser focal spot size was approximately $100 \times 80 \mu\text{m}^2$, and oversampling was employed for LDI imaging. Additional experimental information is provided in the Supporting Information.

Acknowledgements

This material is based upon work supported by the U.S. Department of Energy, Office of Science, Office of Basic Energy Sciences, Chemical Sciences, Geosciences and Biosciences Division under Award Number DE-FG02-01ER15129 to A.V. S.A.S. is appreciative of the scholarship award from the Achievement Rewards for College Scientists Foundation, Inc.

Keywords: mass spectrometry imaging · silicon nanopost array · small-molecule imaging · tissue section

How to cite: *Angew. Chem. Int. Ed.* **2016**, *55*, 4482–4486
Angew. Chem. **2016**, *128*, 4558–4562

- [1] A. Dove, *Science* **2010**, *328*, 920–922.
- [2] M. M. Gessel, J. L. Norris, R. M. Caprioli, *J. Proteomics* **2014**, *77*, 71–82.
- [3] A. McEwen, C. Henson, *Bioanalysis* **2015**, *7*, 557–568.
- [4] A. Roempp, S. Guenther, Y. Schober, O. Schulz, Z. Takats, W. Kummer, B. Spengler, *Angew. Chem. Int. Ed.* **2010**, *49*, 3834–3838; *Angew. Chem.* **2010**, *122*, 3923–3927.
- [5] B. Spengler, *Anal. Chem.* **2015**, *87*, 64–82.

- [6] S. G. Boxer, M. L. Kraft, P. K. Weber, *Annu. Rev. Biophys.* **2009**, *38*, 53–74.
- [7] D. S. Cornett, M. L. Reyzer, P. Chaurand, R. M. Caprioli, *Nat. Methods* **2007**, *4*, 828–833.
- [8] T. A. Zimmerman, S. S. Rubakhin, J. V. Sweedler, *J. Am. Soc. Mass Spectrom.* **2011**, *22*, 828–836.
- [9] J. Krismer, J. Sobek, R. F. Steinhoff, S. R. Fagerer, M. Pabst, R. Zenobi, *Appl. Environ. Microbiol.* **2015**, *81*, 5546–5551.
- [10] J. M. Wiseman, D. R. Ifa, Q. Song, R. G. Cooks, *Angew. Chem. Int. Ed.* **2006**, *45*, 7188–7192; *Angew. Chem.* **2006**, *118*, 7346–7350.
- [11] E. R. Amstalden van Hove, D. F. Smith, R. M. A. Heeren, *J. Chromatogr.* **2010**, *1217*, 3946–3954.

- [12] N. Bergman, D. Shevchenko, J. Bergquist, *Anal. Bioanal. Chem.* **2014**, *406*, 49–61.
- [13] J. Sunner, E. Dratz, Y. C. Chen, *Anal. Chem.* **1995**, *67*, 4335–4342.
- [14] S. F. Ren, L. Zhang, Z. H. Cheng, Y. L. Guo, *J. Am. Soc. Mass Spectrom.* **2005**, *16*, 333–339.
- [15] R. Nayak, D. R. Knapp, *Anal. Chem.* **2007**, *79*, 4950–4956.
- [16] S. Nitta, H. Kawasaki, T. Suganuma, Y. Shigeri, R. Arakawa, *J. Phys. Chem. C* **2013**, *117*, 238–245.
- [17] S. Szunerits, Y. Coffinier, R. Boukherroub, *Sensors* **2015**, *15*, 12573.
- [18] R. Nayak, D. R. Knapp, *Anal. Chem.* **2010**, *82*, 7772–7778.
- [19] T. Watanabe, H. Kawasaki, T. Yonezawa, R. Arakawa, *J. Mass Spectrom.* **2008**, *43*, 1063–1071.
- [20] M. C. Bernier, V. H. Wysocki, S. Dagan, *J. Mass Spectrom.* **2015**, *50*, 891–898.
- [21] J. Wei, J. M. Buriak, G. Siuzdak, *Nature* **1999**, *399*, 243–246.
- [22] S. A. Trauger, E. P. Go, Z. X. Shen, J. V. Apon, B. J. Compton, E. S. P. Bouvier, M. G. Finn, G. Siuzdak, *Anal. Chem.* **2004**, *76*, 4484–4489.
- [23] T. R. Northen, O. Yanes, M. T. Northen, D. Marrinucci, W. Uritboonthai, J. Apon, S. L. Golledge, A. Nordstrom, G. Siuzdak, *Nature* **2007**, *449*, 1033–U1033.
- [24] K. Qian, L. Zhou, J. Liu, J. Yang, H. Y. Xu, M. H. Yu, A. Nouwens, J. Zou, M. J. Monteiro, C. Z. Yu, *Sci. Rep.* **2013**, *3*, 1415.
- [25] C. Li, Z. Z. Wang, A. D. Jones, *Anal. Bioanal. Chem.* **2014**, *406*, 171–182.
- [26] D. N. de Oliveira, M. S. Ferreira, R. R. Catharino, *PLoS One* **2014**, *9*, e90901.
- [27] A. Tata, C. Montemurro, A. M. Porcari, K. C. Silva, J. B. L. de Faria, M. N. Eberlin, *Drug Test. Anal.* **2014**, *6*, 949–952.
- [28] V. L. Brown, Q. Liu, L. He in *Mass Spectrometry Imaging of Small Molecules*, Vol. 1203 (Ed.: L. He), Humana Press, New York, NY, USA, **2015**, pp. 175–184.
- [29] C. López de Laorden, A. Beloqui, L. Yate, J. Calvo, M. Puigivilla, J. Llop, N.-C. Reichardt, *Anal. Chem.* **2015**, *87*, 431–440.
- [30] D. Y. Lee, V. Platt, B. Bowen, K. Louie, C. A. Canaria, C. T. McMurray, T. Northen, *Integr. Biol.* **2012**, *4*, 693–699.
- [31] G. J. Patti, L. P. Shriver, C. A. Wassif, H. K. Woo, W. Uritboonthai, J. Apon, M. Manchester, F. D. Porter, G. Siuzdak, *Neuroscience* **2010**, *170*, 858–864.
- [32] P. J. O'Brien, M. Lee, M. E. Spilker, C. C. Zhang, Z. Yan, T. C. Nichols, W. Li, C. H. Johnson, G. J. Patti, G. Siuzdak, *Cancer Metab.* **2013**, *1*, 4–4.
- [33] M. P. Greving, G. J. Patti, G. Siuzdak, *Anal. Chem.* **2011**, *83*, 2–7.
- [34] B. N. Walker, J. A. Stolee, D. L. Pickel, S. T. Retterer, A. Vertes, *J. Phys. Chem. C* **2010**, *114*, 4835–4840.

- [35] J. A. Stolee, B. N. Walker, V. Zorba, R. E. Russo, A. Vertes, *Phys. Chem. Chem. Phys.* **2012**, *14*, 8453–8471.
- [36] B. N. Walker, J. A. Stolee, A. Vertes, *Anal. Chem.* **2012**, *84*, 7756–7762.
- [37] N. J. Morris, H. Anderson, B. Thibeault, A. Vertes, M. J. Powell, T. T. Razunguzwa, *RSC Adv.* **2015**, *5*, 72051–72057.
- [38] B. N. Walker, C. Antonakos, S. T. Retterer, A. Vertes, *Angew. Chem. Int. Ed.* **2013**, *52*, 3650–3653; *Angew. Chem.* **2013**, *125*, 3738–3741.
- [39] B. N. Walker, T. Razunguzwa, M. Powell, R. Knochenmuss, A. Vertes, *Angew. Chem. Int. Ed.* **2009**, *48*, 1669–1672; *Angew. Chem.* **2009**, *121*, 1697–1700.
- [40] J. A. Stolee, A. Vertes, *Phys. Chem. Chem. Phys.* **2011**, *13*, 9140–9146.
- [41] O. Yanes, H.-K. Woo, T. R. Northen, S. R. Oppenheimer, L. Shriver, J. Apon, M. N. Estrada, M. J. Potchoiba, R. Steenwyk, M. Manchester, G. Siuzdak, *Anal. Chem.* **2009**, *81*, 2969–2975.
- [42] B. N. Walker, J. A. Stolee, D. L. Pickel, S. T. Retterer, A. Vertes, *Appl. Phys. A* **2010**, *101*, 539–544.
- [43] J. V. Small, T. Stradal, E. Vignal, K. Rottner, *Trends Cell Biol.* **2002**, *12*, 112–120.
- [44] R. A. Kruse, S. S. Rubakhin, E. V. Romanova, P. W. Bohn, J. V. Sweedler, *J. Mass Spectrom.* **2001**, *36*, 1317–1322.

Received: December 16, 2015

Published online: March 1, 2016

Supporting Information

Molecular Imaging of Biological Samples on Nanophotonic Laser Desorption Ionization Platforms

*Sylwia A. Stopka, Charles Rong, Andrew R. Korte, Sridevi Yadavilli, Javad Nazarian, Trust T. Razunguzwa, Nicholas J. Morris, and Akos Vertes**

anie_201511691_sm_miscellaneous_information.pdf

MATERIALS AND METHODS

Imaging chip nanofabrication. NAPA surfaces were fabricated using low resistivity (0.001 – 0.005 ohm-cm) <100> p-type silicon wafers. Wafers were spin-coated with anti-reflective coating (AR2-600, DOW Shipley, Marlborough, MA, USA) at 3500 rpm for 30 s and baked on a hot plate at 220 °C for 1 min. Negative-tone DUV photoresist (UVN-2300, DOW Shipley, Marlborough, MA, USA) was then spin-coated at 3500 rpm for 30 s. A soft bake was performed on a hot plate at 110 °C for 90 s. Projection exposure of the nanopost pattern was achieved using a 248 nm wavelength DUV stepper (ASML 5500/300, ASML, Veldhoven, The Netherlands) with 4× reduction optics. A post exposure bake followed at 105 °C for 60 s. The resulting pattern of 150 nm diameter circles with a periodicity of 337 nm was developed (AZ300MIF, Clariant, Somerville, NJ, USA) for 22 s. After developing, wafers were rinsed in deionized water for 60 s and dried using N₂ gas.

Etching was performed using a deep reactive ion etcher chamber (DRIE, PlasmaTherm, St. Petersburg, FL, USA). A single-step vertical Si etch was performed with a chamber pressure of 19 mTorr, an ICP power of 825 W and an RIE power of 15 W for 9 min. The mixture of etchant gases was as follows: C₄F₈, SF₆, and Ar at 52 sccm, 28 sccm, and 20 sccm, respectively. Wafers were etched to a depth of 1100 nm. A post-etch oxygen plasma clean (Technics PEII, Technics, Pleasanton, CA, USA) was performed for 3 min at 300 mTorr chamber pressure and 100 W to remove any residual photoresist from the nanoposts. Characterization was performed by scanning-electron microscopy (JSM-7600F, JEOL, Peabody, MA, USA).

Animals and tissue preparation. All animal work was performed in accordance with the approved institutional animal use and care protocol (CNMC protocol # 30425). Nude mice (J:NU) were purchased from Jackson Laboratories (Bar Harbor, ME, USA) and were maintained in conventional animal housing rooms. Six month old healthy mice were euthanized by CO₂ asphyxiation and whole brain and kidney were collected immediately by cutting through the skin and opening the cranium and the abdominal cavity, respectively. The organs were quickly rinsed in 1 × PBS, and frozen immediately by placing them in a chilled tube that was kept on dry ice. The frozen brain and kidney were stored at -80 °C until the time of sectioning. For cryosectioning, the organs were placed into the cryostat chamber (CM1800, Leica Microsystems Inc., Nussloch, Germany) for at least 30 min to allow thermal equilibration. The organs then were mounted using a few drops of distilled water to freeze them onto the sample mount. Mouse brains and kidneys were sectioned at -23 °C and -21 °C, respectively, to 10 µm thickness using an anti-roll system to limit sample tearing. Coronal cuts were obtained from the mouse brain and sagittal sections were taken from the kidneys. The sections were transferred by thaw-mounting onto a NAPA imaging chip, and immediately placed inside a vacuum chamber (~75 Torr) for ~10 min until the sample dried. Lastly, the NAPA chip containing the sample was mounted on a MALDI plate using double sided carbon tape.

Cells cultured on NAPA. Human hepatocarcinoma cells (Hep G2/C3A, strain CRL-10741, ATCC, Manassas, VA, USA) were cultured in supplemented Eagle's Minimum Essential Medium (EMEM) with 10% fetal bovine serum and 1% penicillin-streptomycin.

Prior to culturing, the 4 mm² area NAPA chips were first sterilized with 70% ethanol. An initial cell density of $\sim 5.0 \times 10^4$ cells/mL was seeded on the NAPA substrates, by dispensing 15 μ L cell solution corresponding to ~ 750 cells. The inoculated NAPA chip was cultured for one hour at 37 °C and 5% CO₂ in an incubator (HERAcell 150i, Thermo Scientific, Waltham, MA, USA) using 35 mm culture dishes. After the cells attached to the silicon substrate, 2 mL of EMEM medium was added to the culture dish containing the NAPA chip. Cell growth was monitored periodically with an optical microscope. Prior to LDI-MSI from the NAPA chip, a gentle stream of DI water was used to rinse off any excess medium.

NAPA imaging. Tissue sections and cells were analyzed in both positive and negative ion modes, using a linear ion trap-orbitrap hybrid mass spectrometer with a MALDI ion source (MALDI LTQ-Orbitrap XL, Thermo Fisher Scientific Inc., Bremen, Germany) equipped with a nitrogen laser (337 nm and 60 Hz repetition rate). Depending on the thickness and sample type, laser fluences used for imaging experiments ranged between 13 and 100 mJ/cm². Spectra were acquired using 2 to 10 shots for each pixel. As the laser focal spot size was $\sim 100 \mu\text{m} \times 80 \mu\text{m}$, for oversampling 50 μm step size was used, unless otherwise noted. The automatic gain control function was not utilized during any of the experiments. Mass resolving power was varied from 30,000 to 100,000. On average an increase in the number of spectral features from ~ 200 to ~ 300 was observed, which allowed for the corresponding MSI mapping of nearly isobaric lipid ions with Δm of ~ 20 mDa (see Figure S5).

Data processing. For data analysis, Xcalibur (3.0.63) and ImageQuest (1.1.0) (Thermo Fisher Scientific Inc., Bremen, Germany) were used to interpret the spectra and imaging datasets, respectively. For visualization, unsmoothed data was displayed on a logarithmic intensity scale and the color scale was normalized. For tandem MS during imaging, a four scan raster pattern was used, in which the first scan was a full mass spectrum acquired in the Orbitrap analyzer. The subsequent three steps were data-dependent MS/MS scans, acquired in the ion trap analyzer, with ions selected for fragmentation based on the high-resolution MS scan in the first step. Normalized collision energies in the latter scans were ramped from 30 to 70 units, with an isolation window of ± 0.75 . Putative annotation of metabolites was based on accurate mass measurements, molecular formulas, and tandem mass spectra, searched against the Metlin and LipidMaps databases.

Algal cell cultures. Wild type *Chlamydomonas reinhardtii* (CC125) was purchased from the Chlamydomonas Resource Center at the University of Minnesota. Cells were inoculated in tris acetate phosphate medium and incubated at 27 °C and 80 RPM in an orbital shaker. This process is explained in further detail elsewhere.^[1] Illumination was provided by LED lights installed above the culture and maintained at $100 \mu\text{mol m}^{-2}\text{s}^{-1}$ and cycled at 12 h / 12 h light/dark by a digital timer. Cells were sampled by harvesting 1 mL of cell solution and adjusted to a final concentration of $\sim 10^6$ cells/mL, then pelleted at $2000\times g$ for 2 min. The medium was removed and cells were washed with DI water. A volume of 500 nL of cell suspension was loaded onto a 4 mm^2 NAPA chip, allowed to air dry, and placed onto a MALDI plate for LDI-MS analysis.

ADDITIONAL RESULTS

Analysis of small cell clusters. In addition to tissue imaging, NAPA-LDI-MSI can be used for the high-throughput analysis of small cell clusters. Live *Chlamydomonas reinhardtii* cells were deposited onto a NAPA chip, dried, transferred into the mass spectrometer, and imaged using a laser fluence of ~ 60 mJ/cm². Overlaying resulting chemical images (see Figure S6a) for ions such as [DG(40:4)+NH₄]⁺, [DGTS(32:0)+H]⁺, and porphyrins [chlorophyll *a* and *b*+H]⁺ (see Figure S6b) on the optical image allowed for coregistration of cellular coordinates in the latter, and MSI pixels and mass spectra.

The number of spectral features was also found to increase with the number of cells. For example, pixels that contained 10, 50, and 80 cells showed 80, 120, and 210 spectral features, respectively. The mass spectra were free of background ions as shown by a spectrum from a 50-cell pixel (see Figure S6c). The signal intensity for the four metabolites was found to correlate with the number of cells within a given MSI pixel. The intensities of ions [DG(40.4)+NH₄]⁺, [DGTS(32:0)+H]⁺, [chlorophyll *a*+H]⁺ and [chlorophyll *b*+H]⁺ were proportional with the numbers of cells in the range between 20 to 80 cells per pixel (see Figure S6d).

SUPPORTING FIGURES

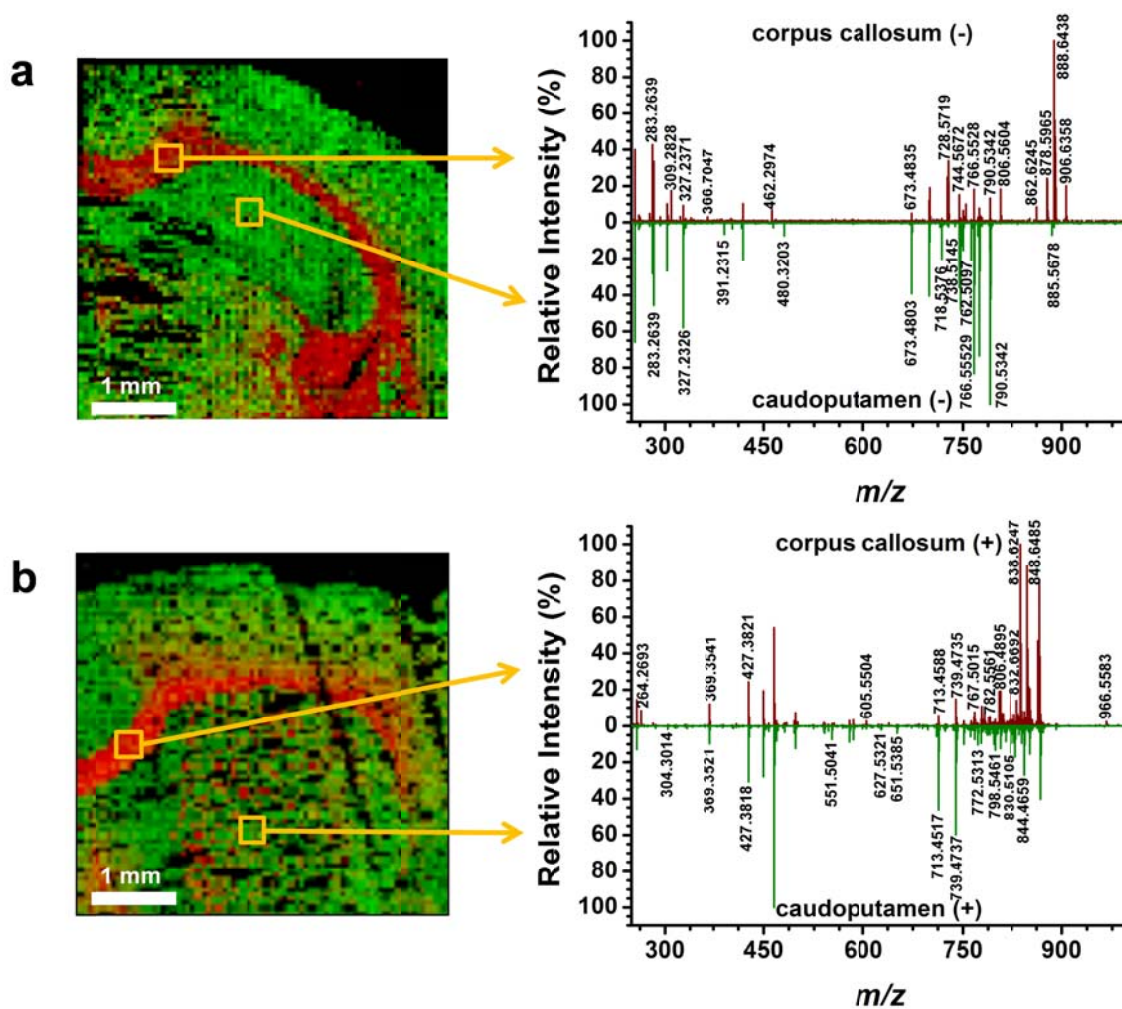


Figure S1. (a) Composite image (left) of negative ion distributions from NAPA-LDI-MSI of a coronal mouse brain section showing the intensities of m/z 888.6438 (red) and m/z 790.5342 (green). The regions demarcated by the orange box in the corpus callosum (CC) and caudoputamen (CP) show the areas averaged from 30 scans to obtain the spectra presented on the right. (b) A composite image of positive ion intensities for m/z 848.6485 (red) and m/z 739.4737 (green) using NAPA-LDI-MSI of a coronal brain section. On the right, an average of 30 individual scans is shown from the regions selected in the CC and CP.

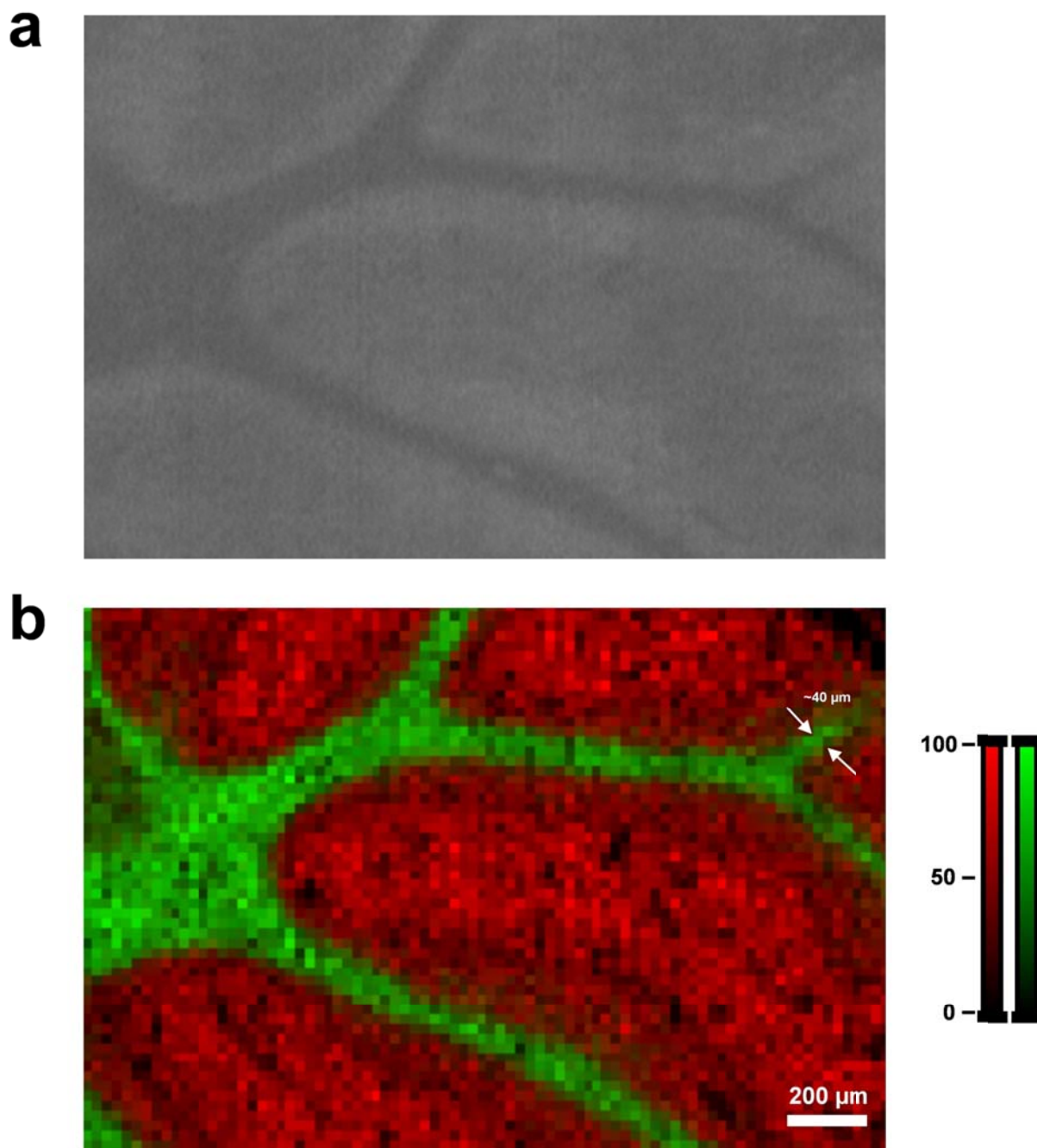


Figure S2. (a) In-source optical image of a 10 μm -thick mouse cerebellum section acquired using the camera of the mass spectrometer. (b) Composite plot showing intensity distributions for PA(18:1/16:0) in red and GlcCer(24:1) in green. The narrowest discernible molecular features indicated by arrows are $\sim 40 \mu\text{m}$ in size.

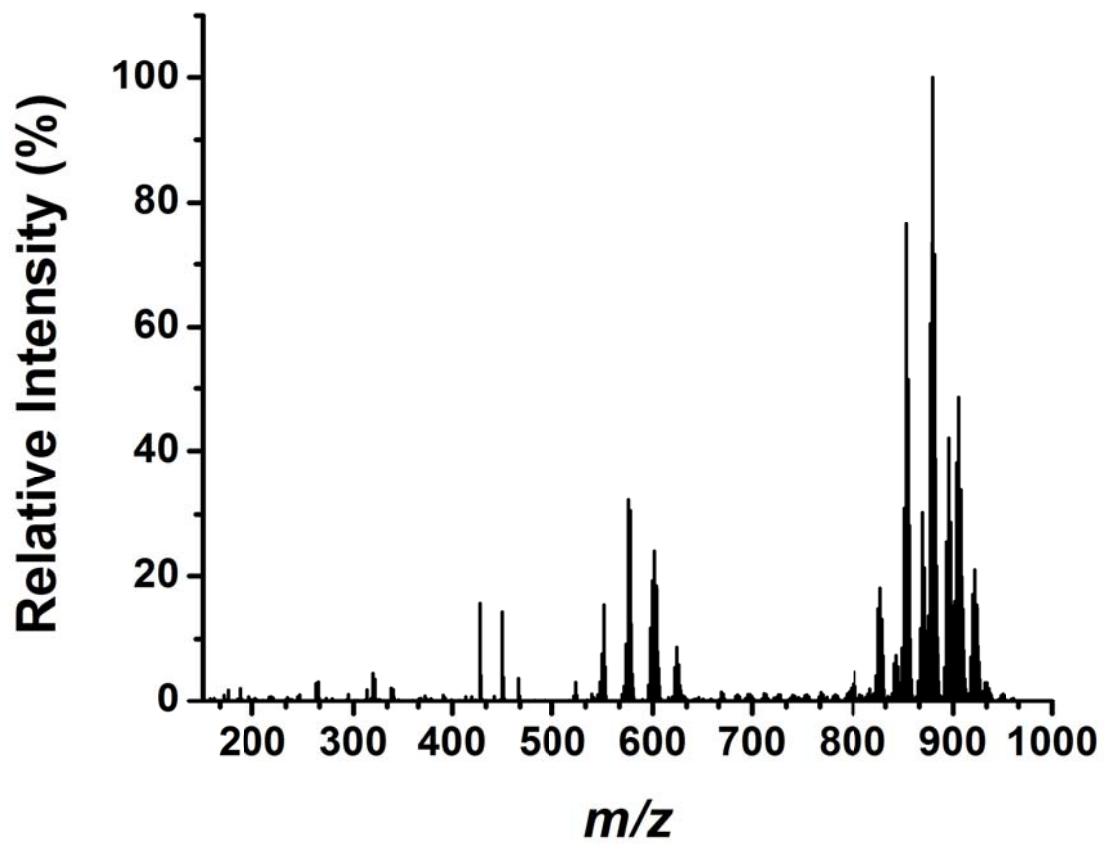


Figure S3. Average of 15 positive ion mode NAPA-LDI-MS scans obtained from mouse kidney section shows negligible background peaks.

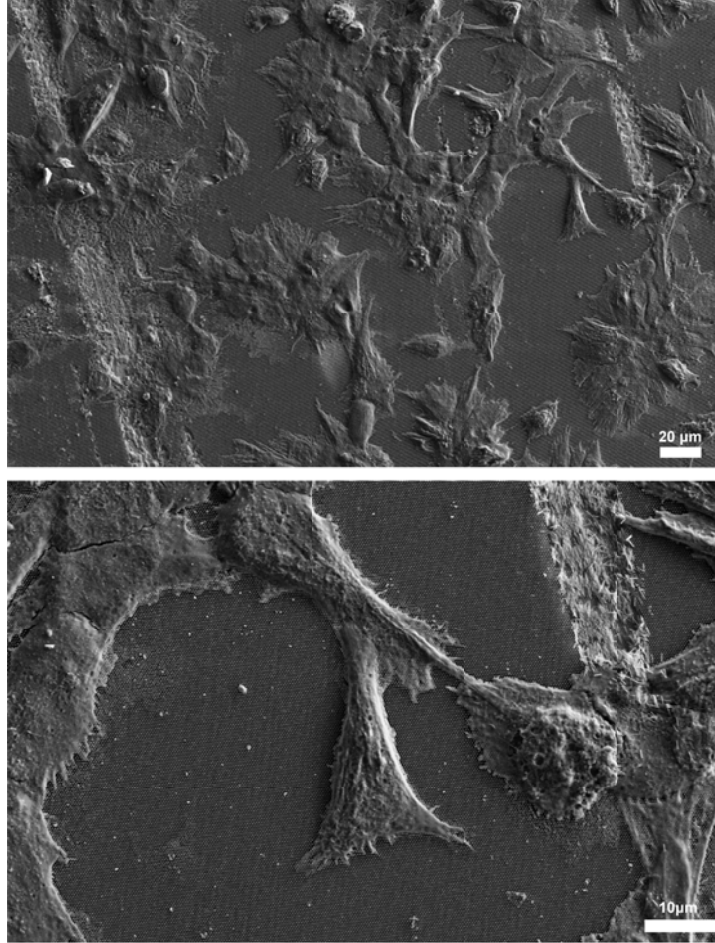


Figure S4. SEM images of HepG2/C3A cells cultured on NAPA substrate after six days. The cells adhered to the nanostructure and exhibited regular lamellipodia.

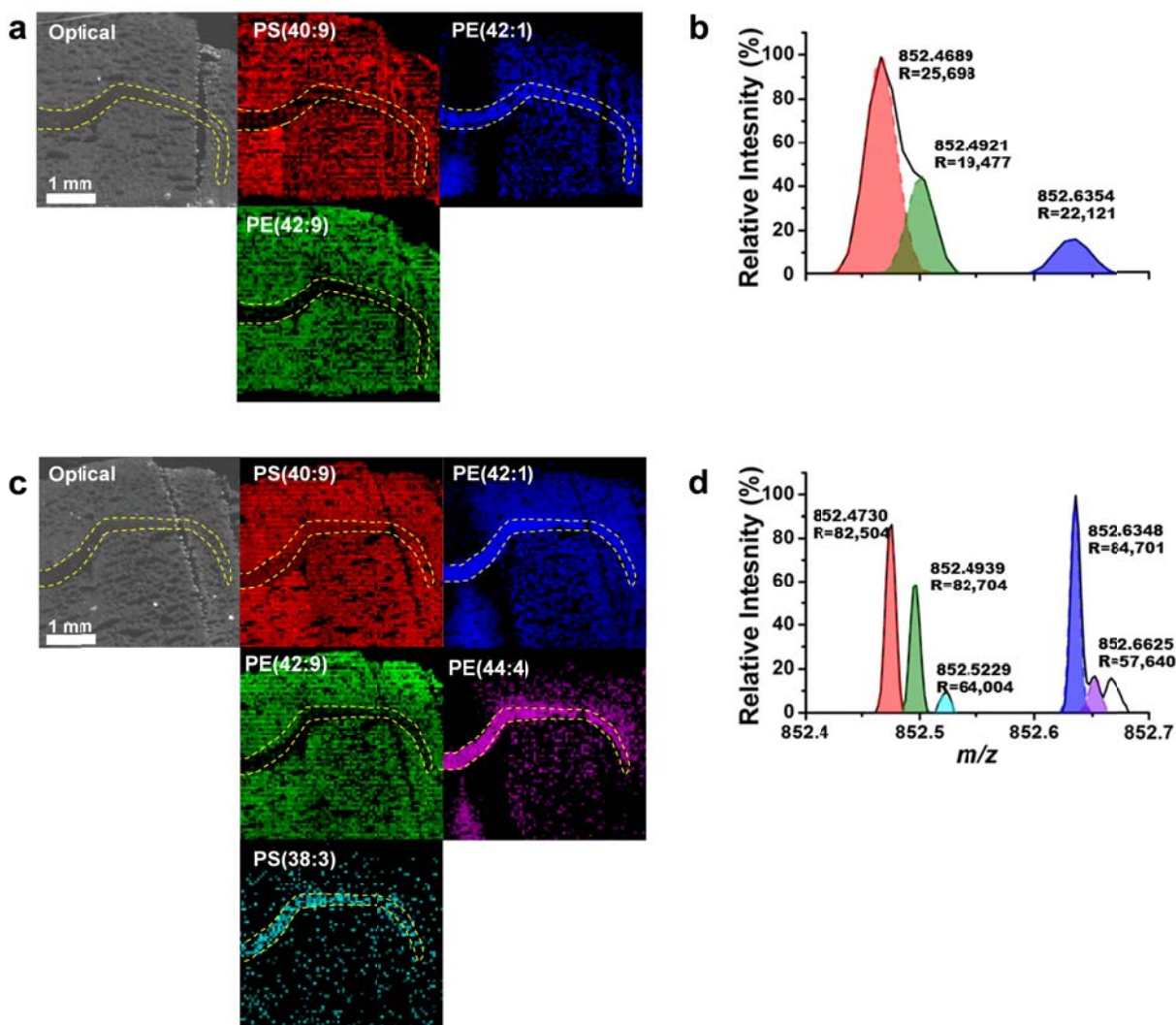


Figure S5. Optical and MS images obtained by positive mode NAPA-LDI-MSI from a coronal mouse brain section using a resolving power of (a) 30,000 and (c) 100,000. (b) At the lower resolving power, only three peaks appeared around nominal m/z 852, two of which were poorly resolved. (d) As mass resolution increased, the five underlying ions were discerned and the corresponding images (see panel (c)) revealed more accurate distributions.

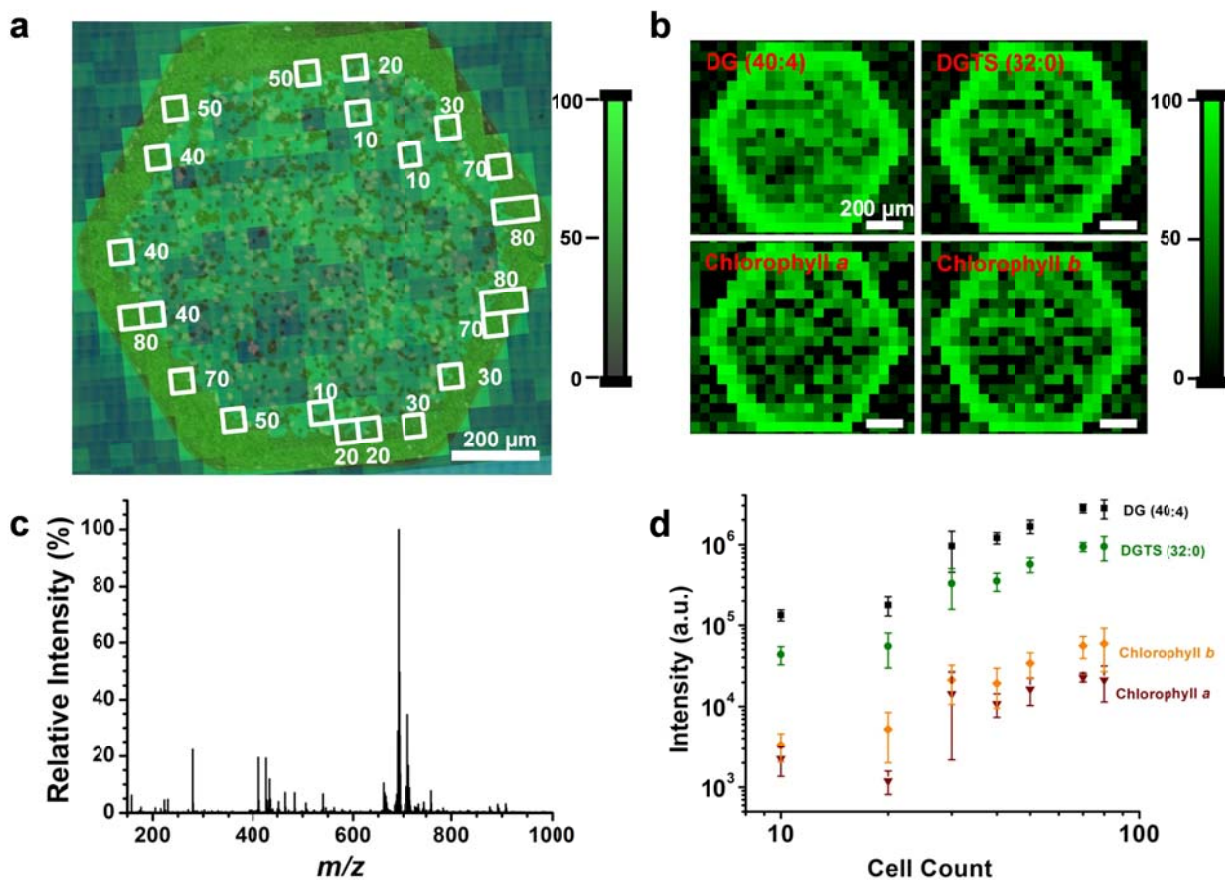


Figure S6. Analysis of small cell populations as a function of cluster size and localization is demonstrated by LDI-MS imaging of *C. reinhardtii* cells on a NAPA platform. (a) DG(40:4) chemical image overlaid on an optical image. Each 50 μm MSI pixel corresponds to the indicated number of cells. (b) NAPA-LDI images of four different ions used to correlate ion intensities with cell numbers in a pixel. (c) Mass spectrum of 50 cells in a single pixel by NAPA-LDI at 60 mJ/cm^2 fluence. (d) Ion intensities are proportional to cell numbers in a given MSI pixel in the 20 to 80 cells/pixel range.

Table S1. Putative annotation of negative ions from mouse brain tissue.

Assignment	Ion	Formula	$m/z_{exp.}$	$m/z_{calc.}$	$\Delta m/z$ (mDa)	Tissue location ^b
Pentadecanoic acid	[M-H] ⁻	C ₁₅ H ₃₀ O ₂	241.2175	241.2167	0.8	
Hexadecenoic acid ^a	[M-H] ⁻	C ₁₆ H ₃₀ O ₂	253.2179	253.2167	1.2	CC, aco
Palmitic acid	[M-H] ⁻	C ₁₆ H ₃₂ O ₂	255.2332	255.2324	0.8	
Octadecadienoic acid	[M-H] ⁻	C ₁₈ H ₃₂ O ₂	279.2330	279.2324	0.6	
Octadecenoic acid ^a	[M-H] ⁻	C ₁₈ H ₃₄ O ₂	281.2484	281.2480	0.4	CC, Ms, aco
Stearic acid ^a	[M-H] ⁻	C ₁₈ H ₃₆ O ₂	283.2639	283.2637	0.2	
Eicosatetraenoic acid	[M-H] ⁻	C ₂₀ H ₃₂ O ₂	303.2327	303.2324	0.3	CTX, CP, LSr
Eicosenoic acid	[M-H] ⁻	C ₂₀ H ₃₈ O ₂	309.2795	309.2790	0.5	CC, Ms, aco
Docosahexaenoic acid	[M-H] ⁻	C ₂₂ H ₃₂ O ₂	327.2335	327.2324	1.1	CTX, CP, LSr
Docosatetraenoic acid	[M-H] ⁻	C ₂₂ H ₃₆ O ₂	331.2648	331.2637	1.1	CC, Ms, LSr, aco
cLPA(16:0)	[M-H] ⁻	C ₁₉ H ₃₇ O ₆ P	391.2272	391.2249	2.3	
Ascorbyl palmitate	[M-H] ⁻	C ₂₂ H ₃₈ O ₇	413.2530	413.2539	-0.9	
CPA(18:1)	[M-H] ⁻	C ₂₁ H ₃₉ O ₆ P	417.2430	417.2411	1.9	
CPA(18:0)	[M-H] ⁻	C ₂₁ H ₄₁ O ₆ P	419.2587	419.2568	1.9	
LPI(18:0)	[M-H] ⁻	C ₂₂ H ₅₃ O ₁₂ P	599.3242	599.3196	4.6	
GlcCer(32:0)	[M-H] ⁻	C ₃₈ H ₇₃ NO ₈	670.5223	670.5257	-3.4	CC, aco, Ms
PA(34:1)	[M-H] ⁻	C ₃₇ H ₇₁ O ₈ P	673.4856	673.4808	4.8	CTX, Ms, LSr
PA(18:1/18:1) ^a	[M-H] ⁻	C ₃₉ H ₇₃ O ₈ P	699.5003	699.4970	3.3	CTX, Ms, LSr
PA(18:0/18:1) ^a	[M-H] ⁻	C ₃₉ H ₇₅ O ₈ P	701.5174	701.5121	5.3	CC, Ms, aco
PE-Cer(38:1)	[M-H] ⁻	C ₄₀ H ₈₁ N ₂ O ₆ P	715.5800	715.5753	4.7	
PE(34:0)	[M-H] ⁻	C ₃₉ H ₇₈ NO ₈ P	718.5453	718.5392	6.1	CTX, Ms, LSr
PE(P-36:4)	[M-H] ⁻	C ₄₁ H ₇₄ O ₇ P	722.5177	722.5124	5.3	
PE(O-18:2/18:1) ^a	[M-H] ⁻	C ₄₁ H ₇₈ NO ₇ P	726.5483	726.5443	4.0	CC, Ms, aco
PE(O-18:1/18:1) ^a	[M-H] ⁻	C ₄₁ H ₈₀ NO ₇ P	728.5640	728.5594	4.6	CC, Ms, aco
PE(36:2)	[M-H] ⁻	C ₄₁ H ₇₈ O ₈ NP	742.5455	742.5386	6.9	
PE(16:0/18:1) ^a	[M-H] ⁻	C ₄₁ H ₈₀ NO ₈ P	744.5588	744.5543	4.5	CC, Ms, aco
PE(P-38:6) ^a	[M-H] ⁻	C ₄₃ H ₇₄ NO ₇ P	746.5180	746.5124	5.6	CTX, CP
PE(38:5)	[M-H] ⁻	C ₄₃ H ₇₆ NO ₇ P	748.5323	748.5281	4.2	CTX, CP, Ms
PE(P-38:4) ^a	[M-H] ⁻	C ₄₃ H ₇₈ NO ₇ P	750.5492	750.5437	5.5	CTX, CP, Ms
PE(38:2)	[M-H] ⁻	C ₄₃ H ₈₂ NO ₇ P	754.5805	754.5750	5.5	
PE(22:6/16:0) ^a	[M-H] ⁻	C ₄₃ H ₇₄ NO ₈ P	762.5131	762.5074	5.7	CTX, CP, Ms, LSr
PE(18:0/20:4) ^a	[M-H] ⁻	C ₄₃ H ₇₈ NO ₈ P	766.5446	766.5386	6.0	CTX, CP, Ms, LSr
PE(P-22:6/18:0) ^a	[M-H] ⁻	C ₄₅ H ₇₈ NO ₇ P	774.5496	774.5437	5.9	CTX, CP, Ms, LSr
PE(P-40:5)	[M-H] ⁻	C ₄₅ H ₈₀ NO ₇ P	776.5643	776.5594	4.9	CTX, CP, Ms, LSr

PE(22:6/18:0) ^a	[M-H] ⁻	C ₄₅ H ₇₈ NO ₈ P	790.5448	790.5386	6.2	CTX, CP, LSr
PE(44:4)	[M-H] ⁻	C ₄₉ H ₉₀ NO ₈ P	850.6297	850.6326	-2.9	CC, aco
PE(44:3)	[M-H] ⁻	C ₄₉ H ₉₂ NO ₈ P	852.6448	852.6482	-3.4	CC
ST(22:0-OH) ^a	[M-H] ⁻	C ₄₆ H ₈₉ NO ₁₂ S	878.6077	878.6032	4.5	CC, aco
PI(20:4/18:0) ^a	[M-H] ⁻	C ₄₇ H ₈₃ O ₁₃ P	885.5559	885.5490	6.9	CC, aco
ST(24:1) ^a	[M-H] ⁻	C ₄₈ H ₉₁ NO ₁₁ S	888.6277	888.6285	-0.8	CC, Ms, aco
ST(24:0-OH) ^a	[M-H] ⁻	C ₄₈ H ₉₃ NO ₁₂ S	906.6407	906.6340	6.7	CC, Ms, aco

^aChemical species assigned based on tandem MS from NAPA-LDI imaging of tissue section.

^bCC – corpus callosum, CTX – cortex, Ms – medial septal nucleus, NDB – diagonal band nucleus, CP – caudoputamen, LSr – lateral septal nucleus, and aco – anterior commissure

Table S2. Putative annotation of positive ions from mouse brain tissue.

Assignment	Ion	Formula	$m/z_{exp.}$	$m/z_{calc.}$	$\Delta m/z$ (mDa)	Tissue location ^b
Phosphocholine ^a	[M+H] ⁺	C ₅ H ₁₄ NO ₄ P	184.0732	184.0733	-0.1	
Glucose ^a	[M+Na] ⁺	C ₆ H ₁₂ O ₆	203.0525	203.0526	-0.1	
Cholesterol ^a	[M-H ₂ O+H] ⁺	C ₂₇ H ₄₆ O	369.3516	369.3521	-0.5	
LPC(16:2) ^a	[M+H] ⁺	C ₂₄ H ₄₈ NO ₆ P	478.3287	478.3292	-0.5	CTR, CP, LSr
LPC(O-18:2)	[M+H] ⁺	C ₂₆ H ₅₂ NO ₆ P	506.3602	506.3605	-0.3	
Cer(36:1)	[M-H ₂ O+H] ⁺	C ₃₆ H ₇₁ NO ₃	530.5291	530.5306	-1.5	CP, LSr
LPC(17:0)	[M+K] ⁺	C ₂₅ H ₅₀ NO ₇ P	546.2964	546.2956	0.8	
DG(P-32:1)	[M+H] ⁺	C ₃₅ H ₆₆ O ₄	551.5029	551.5034	-0.5	CTX, CP, LSr
DG(36:3)	[M-H ₂ O+H] ⁺	C ₃₉ H ₇₀ O ₅	601.5197	601.5196	0.1	
DG(36:2)	[M-H ₂ O+H] ⁺	C ₃₉ H ₇₂ O ₅	603.5345	603.5352	-0.7	
DG(36:1)	[M-H ₂ O+H] ⁺	C ₃₇ H ₇₄ O ₅	605.5502	605.5509	-0.7	CTX, CC, aco
Heme B ^a	[M] ⁺	C ₃₄ H ₃₂ O ₄ N ₄ Fe	616.1771	616.1773	-0.2	
PA(O-35:2)	[M+H] ⁺	C ₃₈ H ₇₃ O ₇ P	673.5163	673.5167	-0.4	CTX, CP, LSr
PC(32:0)	[M-N(CH ₃) ₃ +Na] ⁺	C ₃₇ H ₇₁ O ₈ P	697.4775	697.4779	-0.4	CTX, CP, LSr
PC(32:1)	[M-N(CH ₃) ₃ +K] ⁺	C ₃₇ H ₆₉ O ₈ P	711.4379	711.4362	1.7	CTX, CP, LSr
PC(32:0)	[M-N(CH ₃) ₃ +K] ⁺	C ₃₇ H ₇₁ O ₈ P	713.4517	713.4518	-0.1	CTX, CP, LSr
PC(34:1)	[M-N(CH ₃) ₃ +Na] ⁺	C ₃₉ H ₇₃ O ₈ P	723.4930	723.4935	-0.5	CTX, CP, LSr
PC(34:1)	[M-N(CH ₃) ₃ +K] ⁺	C ₃₉ H ₇₃ O ₈ P	739.4679	739.4675	0.4	CTX, CP, LSr
PC(32:0)	[M+Na] ⁺	C ₄₀ H ₈₀ NO ₈ P	756.5517	756.5514	0.3	CTX, CP, LSr
PA(38:5)	[M+K] ⁺	C ₄₁ H ₇₁ O ₈ P	761.4510	761.4518	-0.8	CTX, CP, LSr
PA(38:2)	[M+K] ⁺	C ₄₁ H ₇₇ O ₈ P	767.4981	767.4988	-0.7	CTX, CC, CP, aco
PC(32:1)	[M+K] ⁺	C ₄₀ H ₇₈ NO ₈ P	770.5136	770.5097	3.9	CTX, CP, LSr, aco
PC(32:0)	[M+K] ⁺	C ₄₀ H ₈₀ NO ₈ P	772.5253	772.5253	0.0	CTX, CP, LSr, aco
PC(18:0/16:1) ^a	[M+Na] ⁺	C ₄₂ H ₈₂ NO ₈ P	782.5601	782.5670	-6.9	CC, aco, Ms, NDB
PE(P-38:6)	[M+K] ⁺	C ₄₃ H ₇₄ NO ₇ P	786.4810	786.4834	-2.4	CTX, CP, LSr
PE(P-38:5)	[M+K] ⁺	C ₄₃ H ₇₆ NO ₇ P	788.4962	788.4991	-2.9	CC, aco,
PE(P-38:4)	[M+K] ⁺	C ₄₃ H ₇₈ NO ₇ P	790.5126	790.5147	-2.1	CC, LSr, aco
PC(34:1)	[M+K] ⁺	C ₄₂ H ₈₂ NO ₈ P	798.5408	798.5410	-0.2	CTX, LSr
PE(38:6)	[M+K] ⁺	C ₄₃ H ₇₄ NO ₈ P	802.4768	802.4784	-1.6	CTX, LSr
GlcCer(36:2)	[M+K] ⁺	C ₄₄ H ₈₃ NO ₉	808.5714	808.5699	1.5	CC, aco
PI-Cer(18:0/18:0) ^a	[M+H] ⁺	C ₄₂ H ₈₄ NO ₁₁ P	810.5853	810.5855	-0.2	CC, aco
PE(P-40:6)	[M+K] ⁺	C ₄₅ H ₇₈ NO ₇ P	814.5139	814.5147	-0.8	CTX, LSr
PE(P-40:4)	[M+K] ⁺	C ₄₅ H ₈₂ NO ₇ P	818.5450	818.5460	-1.0	CC, aco
PC(36:4)	[M+K] ⁺	C ₄₄ H ₈₀ NO ₈ P	820.5296	820.5253	4.3	CTX, LSr
GlcCer(24:1)	[M+Na] ⁺	C ₄₈ H ₉₁ NO ₈	832.6642	832.6636	0.6	CC, aco
PI-Cer(38:0)	[M+H] ⁺	C ₄₄ H ₈₈ NO ₁₁ P	838.6168	838.6168	0.0	CC, Ms, aco, NDB
PE(40:4)	[M+K] ⁺	C ₄₅ H ₇₄ NO ₈ P	826.4779	826.4783	-0.4	
PI-Cer(40:1)	[M+H] ⁺	C ₄₆ H ₉₀ NO ₁₁ P	864.6325	864.6324	0.1	CC, Ms, aco, NDB
PI-Cer(40:0)	[M+H] ⁺	C ₄₆ H ₉₂ NO ₁₁ P	866.6485	866.6481	0.4	CC, Ms, aco, NDB

TG(36:2)	[M-H ₂ O+H] ⁺	C ₆₀ H ₉₈ O ₆	897.7345	897.7336	0.9
----------	-------------------------------------	--	----------	----------	-----

^aChemical species assigned based on tandem MS from NAPA-LDI imaging of tissue section.

^bCC – corpus callosum, CTX – cortex, Ms – medial septal nucleus, NDB – diagonal band nucleus, CP – caudoputamen, LSr – lateral septal nucleus, and aco – anterior commissure

Table S3. Comparison of selected figures of merit for NAPA-LDI-MSI and MALDI-MSI.

MSI Method	Spatial Resolution		Mass Range (Da)	Log of Dynamic Range	Limit of Detection	References
	General Use	Achievable				
MALDI	50-200 μm	< 1 μm	< 200,000	< 2	20 nmol	[2] [3] [4] [5] [6] [7] [8]
NAPA-LDI	40 μm	40 μm	< 2,000	> 3	800 zmol	[9] [10]

REFERENCES

- [1] S. A. Stopka, B. Shrestha, E. Marechal, D. Falconet, A. Vertes, *Analyst* **2014**, 139, 5945-5953.
- [2] A. Roempp, B. Spengler, *Histochem. Cell Biol.* **2013**, 139, 759-783.
- [3] B. Spengler, M. Hubert, *J. Am. Soc. Mass Spectrom.* **2002**, 13, 735-748.
- [4] E. R. A. van Hove, D. F. Smith, R. M. A. Heeren, *J. Chromatogr.* **2010**, 1217, 3946-3954.
- [5] A. Bodzon-Kulakowska, P. Suder, *Mass Spectrom. Rev.* **2016**, 35, 147-169.
- [6] D. S. Cornett, M. L. Reyzer, P. Chaurand, R. M. Caprioli, *Nat. Methods* **2007**, 4, 828-833.
- [7] M. M. Gessel, J. L. Norris, R. M. Caprioli, *J. Proteomics* **2014**, 107, 71-82.
- [8] T. W. Randolph, B. L. Mitchell, D. F. McLerran, P. D. Lampe, Z. D. Feng, *Mol. Cell. Proteomics* **2005**, 4, 1990-1999.
- [9] B. N. Walker, J. A. Stolee, A. Vertes, *Anal. Chem.* **2012**, 84, 7756-7762.
- [10] N. J. Morris, H. Anderson, B. Thibeault, A. Vertes, M. J. Powell, T. T. Razunguzwa, *RSC Advances* **2015**, 5, 72051-72057.